Assessing Seasonality in the Surface Urban Heat Island of London

BIN ZHOU

Potsdam Institute for Climate Impact Research, Potsdam, Germany

DIRK LAUWAET, HANS HOOYBERGHS, AND KOEN DE RIDDER

Vlaamse Instelling voor Technologisch Onderzoek, Mol, Belgium

JÜRGEN P. KROPP

Potsdam Institute for Climate Impact Research, and Department of Geo- and Environmental Sciences, University of Potsdam, Potsdam, Germany

DIEGO RYBSKI

Potsdam Institute for Climate Impact Research, Potsdam, Germany

(Manuscript received 26 January 2015, in final form 11 September 2015)

ABSTRACT

This paper assesses the seasonality of the urban heat island (UHI) effect in the Greater London area (United Kingdom). Combining satellite-based observations and urban boundary layer climate modeling with the UrbClim model, the authors are able to address the seasonality of UHI intensity, on the basis of both land surface temperature (LST) and 2-m air temperature, for four individual times of the day (0130, 1030, 1330, and 2230 local time) and the daily means derived from them. An objective of this paper is to investigate whether the UHI intensities that are based on both quantities exhibit a similar hysteresis-like trajectory that is observed for LST when plotting the UHI intensity against the background temperature. The results show that the UrbClim model can satisfactorily reproduce both the observed urban–rural LSTs and 2-m air temperatures as well as their differences and the hysteresis in the surface UHI. The hysteresis-like seasonality is largely absent in both the observed and modeled 2-m air temperatures, however. A sensitivity simulation of the UHI intensity to incoming solar radiation suggests that the hysteresis of the LST can mainly be attributed to the seasonal variation in incoming solar radiation.

1. Introduction

As climate change and urbanization globally continue, studies addressing their reciprocal impacts are gaining growing importance (Kalnay and Cai 2003; Parker 2010; UN-HABITAT 2011). The urban heat island (UHI) effect, observed as an elevated temperature of urban areas relative to rural ones, relates to both challenges and is a persistent focus of urban climate and environmental studies (Arnfield 2003; Stewart and Oke 2012). The UHI effect emerges through 1) land surface modification (reduced albedo, less vegetation, increased roughness, and thermal admittance), which favors heat storage and trapping in the city (Oke 1982), and 2) anthropogenic heat release (from vehicles, buildings, and human metabolism; Ichinose et al. 1999; Sailor and Lu 2004). It can also be caused partially by 3) increased incoming longwave radiation as a consequence of air pollution (Rouse et al. 1973). However, air pollutants mostly have a minor or even negligible influence on the UHI, which has been demonstrated through field measurements (Nunez et al. 2000) and modeling (Estournel et al. 1983; Oke et al. 1991).

Conventionally, the UHI intensity is assessed by using 2-m air temperature data obtained from urban and rural weather stations. The air-temperature-based UHI

Denotes Open Access content.

Corresponding author address: Diego Rybski, Potsdam Institute for Climate Impact Research, P.O. Box 601203, Potsdam 14412, Germany.
E-mail: ca-dr@rybski.de

DOI: 10.1175/JAMC-D-15-0041.1

intensity usually reaches its maximum on clear, calm nights and could be as much as 12°C (Oke 1987). Since the 1970s, remotely sensed surface skin temperature data have been used to study urban climate, including the UHI effect. Constant development in sensor technologies and better understanding of atmospheric physics have remarkably enhanced both the quality and the quantity of data, making a multiscale investigation of urban climate possible (Tomlinson et al. 2011). In the last decades, UHI studies based on thermal remote sensing have increased the knowledge on 1) spatial patterns of UHI and its correlation with diverse contributing variables, for example, sky view factor and vegetation; 2) urban surface energy balance; and, to a lesser extent, 3) surface–air relations (Voogt and Oke 2003; Weng 2009).

However, the surface skin temperature, in general, differs from the 2-m air temperature (Norman and Becker 1995; Jin and Dickinson 2010). Prigent et al. (2003) compared the surface skin temperature with in situ measured air temperatures. They found a positive difference between the surface skin temperature and the air temperature during daytime and a negative difference at night, which they attributed mainly to a quicker response of surface temperatures to solar radiation. Dense vegetation and high soil moisture can diminish the difference by altering the partitioning of surface heat fluxes in favor of the latent heat flux. Moreover, the surface skin temperature and the 2-m air temperature converge under cloudy conditions (Prigent et al. 2003; Gallo et al. 2011).

To systematically quantify the UHI intensity, land cover data have been employed to define the spatial extent of cities as contiguous urban clusters (following Rozenfeld et al. 2008), surrounded by a nonurban belt of equal area (Peng et al. 2012). Combining this urban–nonurban definition with remote sensed land surface temperature (LST) data, Zhou et al. (2013) calculated the UHI intensity—defined as the average temperature in the urban cluster minus the average temperature in the nonurban surroundings (background temperature)—in an automated and systematic manner for all European agglomerations.

One of the findings Zhou et al. (2013) present is the region-specific seasonality of the surface UHI intensity occurring in a large number of cities. Plotting the UHI intensity as a function of the background temperature exhibits a clockwise loop with higher intensities in spring than in fall. The causes of this hysteresis are unclear, and it is unknown if a similar phenomenon also takes place for 2-m air temperature.

Table 1 lists some previous works that documented the seasonal variation of UHI intensities. These studies attribute the seasonality mainly to climate and synoptic conditions, for example, monsoon, wind speed, relative humidity, cloudiness, and vegetation, and to a lesser extent to anthropogenic heat release. However, conclusions such as to what extent each factor determines the seasonality are difficult to generalize, as the studies differ considerably in terms of data used (T_{air} vs surface skin temperature), data acquisition method (automobile traverse, remote sensing, and weather station observation), UHI intensity metrics (daily maximum vs mean), and choice of rural reference (station dependent or fairly arbitrary), as well as the time span of observation (from 1 year to multiyear).

Nevertheless, there are still some features in common: during the day, UHI intensities based on the surface skin temperature measured by satellites are found to be the highest in the wet summer season and weaker in the dry season, whereas the air-temperature-based UHI intensities show less obvious seasonal variations. Weaker UHI intensities are usually observed in windier and cloudier months; that is, the UHI is inversely related to wind speed and cloudiness, as summarized by Arnfield (2003). Recently, Schatz and Kucharik (2014) investigated explicitly the seasonality of UHI in Madison, Wisconsin, by using a densely deployed sensor network. They emphasize the key role of vegetation and snow-cover conditions in shaping the seasonality of UHI intensity, whereas factors such as wind and clouds only fluctuate the seasonality to a certain extent. These findings are consistent with earlier works (Imhoff et al. 2010; Peng et al. 2012).

However, little effort has been made to address seasonality by integrating observations with increasingly more sophisticated urban climate modeling. In this work, we modeled the urban climate of London, United Kingdom, by the urban boundary layer climate model UrbClim (De Ridder et al. 2015). Combined with a standardized methodology for quantifying the UHI (Zhou et al. 2013), we were able to assess the hysteresis of this example.

In brief, the aim of this study is to verify 1) if the model can reproduce the hysteresis in the surface temperatures of London, 2) if the hysteresis effect also occurs in the 2-m air temperature, and 3) if the phase shift between astronomical and meteorological cycle is a plausible explanation for the observed hysteresis effect.

2. Numerical model, experiment setup, and model evaluation

a. *The UrbClim model*

The model simulations in this study were performed with the urban boundary layer climate model UrbClim,

TABLE 1. Selected publications that reported seasonal variations of UHI intensity.

Study	City	Year	Seasonal variation
Jauregui (1997)[a]	Mexico City, Mexico	1994	Maximum nighttime UHI intensity (~5°C) occurred in the dry season (Dec–Jan) and declined to a minimum (~2°C) during the wet months (Aug–Sep). Daytime UHI intensity reached a maximum in Jul (~3°C) and diminished to a minimum (~1°C) in Dec.
Figuerola and Mazzeo (1998)[a]	Buenos Aires, Argentina	1994–97	Maximum UHI intensities were frequently found >4°C in winter and spring with weak wind and low cloudiness, while under strong wind and cloudiness, UHI intensities in winter fell dramatically. As the temperature increased in summer, negative UHI intensities occurred more frequently.
Runnalls and Oke (2000)[a]	Vancouver, British Columbia, Canada	1992–94	The nighttime UHI intensity was greatest in the fall, followed by summer, winter, and spring.
Unger et al. (2001)[a]	Szeged, Hungary	1999–2000	Bimodal with maximum UHI intensity (~4°C) in midspring (Apr–May) and late summer (Aug–Sep), largely diminished in winter (~1.5°C).
Wilby (2003)[a]	London, United Kingdom	1961–90	Nighttime UHI intensity peaked in Aug (~2.2°C) and reached its minimum in Jan (~1.1°C). No remarkable seasonality in the daytime UHI intensity was observed.
Kim and Baik (2005)[a]	Seoul, South Korea	2001–02	Strong nighttime and morning UHI intensity in fall and winter (>4°C), least developed in summer. No obvious seasonal pattern for daytime UHI intensity.
Tran et al. (2006)[b]	Tokyo, Japan	2001–02	Daytime UHI intensity reached its peak (~12°C) around Jul/Aug, followed by a decline until Jan/Feb (~3°C).
Roth (2007)[a,c]	(Sub)tropical cities		In the cities under review, a pronounced seasonal variation of nighttime UHI intensities was found, which was attributed to the dry (maximum) and wet (minimum) seasons.
Zhou and Shepherd (2010)[a]	Atlanta, Georgia	1984–2007	UHI intensity reached its peak in spring (Apr–May), depending on the chosen rural station, at 3° and 3.7°C, respectively, and decreased to 1.43° and 2.6°C in August.
Pongrácz et al. (2010)[b]	Munich, Germany; Milan, Italy; Warsaw, Poland; Budapest, Hungary	2001–03	The daytime UHI intensities reached their peak in summer (Jun–Jul) and diminished in winter (Nov–Feb). Nocturnal UHI intensities remained stable (around 2°–3°C) between Mar and Oct and weakened in winter except in Milan, where a maximum UHI intensity of 4°C occurred in Jan–Feb.
Cui and de Foy (2012)[a,b]	Mexico City	2006	For both skin and air temperatures, maximum nighttime UHI intensities (up to 10°C) appeared during the cold dry season (Nov–Feb), while the minima (>5°C) occurred during the wet season (Jul–Oct). The skin-temperature-based daytime UHI intensities were found to be strongest (~12°C) in the wet season and weakest (even negative) in the dry season, whereas the air temperature based ones had low and relatively invariant values across seasons.

[a] Air temperature based.
[b] Surface skin temperature based.
[c] Review article.

designed to cover agglomeration-scale domains at a very high spatial resolution (De Ridder et al. 2015). UrbClim consists of a land surface scheme containing urban physics coupled to a 3D atmospheric boundary layer module.

The land surface scheme is based on the soil–vegetation–atmosphere transfer scheme of De Ridder and Schayes (1997) but is extended to account for urban surface physics. This urbanization is accomplished by representing the urban surface as a rough impermeable slab, with appropriate values for the albedo, emissivity, thermal conductivity, and volumetric heat capacity. The main feature of the extension of the scheme is the inclusion of a parameterization of the inverse Stanton number, which is known to be much higher in urban areas (Kanda et al. 2007; De Ridder et al. 2012). Further details can be found in De Ridder et al. (2015).

The land surface scheme takes part of its input variables (wind speed, temperature, and specific humidity close to the surface) from values simulated in the

atmospheric boundary layer model, a 3D model of the lower atmosphere, extending to a constant height of 3 km.

The atmospheric boundary layer module is tied to synoptic-scale meteorological fields through the lateral and top boundary conditions to ensure that the synoptic forcing is properly taken into account. This model is represented by conservation equations for horizontal momentum (considering zonal and meridional wind speed components u and v, respectively), potential temperature, specific humidity, and mass (involving the vertical wind speed component w). Pressure fields are not calculated internally but are prescribed from a large-scale host model from which UrbClim receives its boundary conditions; hence, only the synoptic-scale pressure gradient is accounted for. By doing so, we avoid the complexities associated with a full mesoscale meteorological model. More importantly, it allows for the use of much longer time increments in the numerical solver and a lower model top (since no absorbing layer is required to damp gravity waves), which makes the model much faster.

The large-scale driving model specifies the lateral and top boundary conditions, the synoptic-scale pressure gradient, and the downwelling radiation and precipitation—the variables required by the land surface scheme. This one-way nesting approach allows the UrbClim model to account for the effect of synoptic weather on local climate (De Ridder et al. 2015).

Terrain elevation data are taken from the Global Multi-Resolution Terrain Elevation Data 2010 (GMTED2010) dataset (Danielson and Gesch 2011), which has a global coverage and is freely available. The spatial distribution of land cover types, needed for the specification of required land surface parameters, is taken from the 2006 Coordinate Information on the Environment (CORINE) land cover data for Europe (Büttner et al. 2007).

The urban land cover percentage is specified using the urban soil scaling raster data files distributed by the European Environment Agency. Maps of vegetation cover fraction are obtained from the normalized difference vegetation index (NDVI) acquired by the MODIS instrument on board the *Terra* satellite platform. Vegetation cover fraction is specified as a function of the NDVI, using the linear relationship proposed by Gutman and Ignatov (1998), and then interpolated to the model grid.

Model grid cells featuring exclusively nonurban land use types are divided into vegetation and bare soil (the complementary fraction). In the case of grid cells containing urban land use, the urban fraction as derived from the urban soil sealing raster data takes precedence over the NDVI-based fractional vegetation cover data in case both sum to over 100%. In case they sum to less than that, the remaining fraction is assigned to bare soil.

Each of the surface types within a grid cell has its own energy balance and corresponding temperature, although the model employs aggregated values for both the aerodynamic and the thermal roughness length parameters. The urban surface cover has an associated very low thermal roughness length that strongly inhibits the turbulent transfer of heat from the urban substrate to the atmosphere, so that a relatively large share of the available radiant surface energy flux is converted to storage heat rather than to turbulent sensible heating of the atmosphere. This, together with the typically high values of thermal inertia of urban materials, leads to the large storage heat flux values typically observed (or estimated as a residual of the surface energy balance) over urban areas (Piringer et al. 2007).

The urban substrate is represented as a massive slab, which is discretized in six vertical layers, and its specific volumetric heat capacity ($2 \times 10^6\,\mathrm{J\,m^{-3}\,K^{-1}}$) and thermal conductivity ($2\,\mathrm{W\,m^{-1}\,K^{-1}}$) values are in line with values found in the literature for urban areas (see, e.g., Oke 1987; Pielke 2002). Evaporation from the urban surface is included by implementing a fractional surface wetness parameter, which accounts for the amount of water stored on the urban substrate, calculated as the difference between precipitation on the urban fraction and evaporation of the stored water. The maximal fraction of wet surface is set as 0.14, with a maximum storage capacity of $1.17\,\mathrm{kg\,m^{-2}}$. Both parameters have been estimated recently by Wouters et al. (2015).

The evolution of the temperature profile in the soil is calculated using the same heat diffusion equations as those used for the urban slab. The main difference is that, for soil, the volumetric heat capacity and thermal conductivity are functions of soil moisture content, as in De Ridder and Schayes (1997). Water transport in the soil is described by means of Richards' equation (Garratt 1992), accounting for infiltration of rainwater in the soil and the uptake of soil water by plant roots. Here also, the reader is referred to De Ridder and Schayes (1997) for more details.

b. *Experiment setup*

The model described above was applied to simulate a 7-yr period (2006–12) for the wider urban agglomeration of London, driven by meteorological data from the ERA-Interim reanalysis dataset of the European Centre for Medium-Range Weather Forecasts (ECMWF).

The domain was configured with 161×161 grid cells in the horizontal direction, using a spatial resolution of

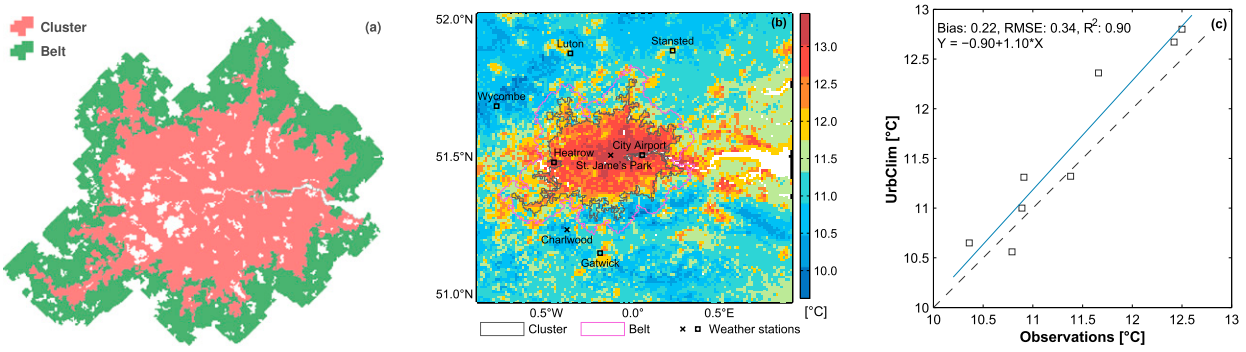

FIG. 1. City cluster and belt for the Greater London area and gridded temperature field. (a) City cluster (pink) identified by city clustering algorithm with $l = 500$ m. The belt (green) is of the same area as the cluster. (b) Modeled annual mean 2-m temperature for the year 2011. The locations of the measurement stations are indicated by black squares, whereas the stations St. James Park and Charlwood are indicated by black times signs. (c) Comparison between observed and modeled annual mean 2-m air temperatures with equation for the straight line.

1 km, equal to the resolution of the MODIS data. In the vertical direction, 20 levels were specified, with the first level 10 m above the displacement height and the resolution smoothly decreasing upward to 250 m at the model top located at 3 km height. This vertical discretization closely matched that of the ECMWF model (De Ridder et al. 2015).

The simulation was initialized on 1 December 2005 at 0000 local time (LT). Initial soil temperature and soil moisture data were taken from the ERA-Interim reanalysis. The sea temperatures in the model were treated separately, and they were adopted from the ERA-Interim reanalysis during the whole simulated period and not calculated internally.

To assess the sensitivity of the observed hysteresis effect in the surface UHI of London to the annual cycle of the incoming shortwave radiation, a sensitivity experiment was carried out. In this scenario, referred to as the SR experiment, the input shortwave radiation from the ERA-Interim reanalysis was rescaled with a daily factor so the clear-sky maximum radiation was always equal to the value of 21 March, when it almost equaled its annual mean value. Thus, all year round, the daily cycle of incoming shortwave radiation under clear-sky conditions remained constant, eliminating the annual cycle. Note that we did not change the temporal variation of the incoming radiation. Cloudy conditions remained cloudy. The values only were rescaled.

3. Data and UHI intensity calculation

We used the same UHI intensity definition as explored by Zhou et al. (2013). The idea is to define a city by its physical extent, that is, via urban land cover. Overlaying the city delineation (and an equal area belt around it) and the heat map, the average temperatures in the city and its surroundings are calculated so that the difference between city and background temperatures (i.e., the belt temperatures) provides the intensity. A similar methodology has been used in prior research (Peng et al. 2012).

In detail, the calculation of the UHI intensity ΔT consists of the following steps:

1) We applied the city clustering algorithm (Rozenfeld et al. 2008, 2011) to CORINE land cover data at 250-m resolution. The algorithm assigns any two urban cells to the same urban cluster if their distance is lower than or equal to a threshold distance l. As in Zhou et al. (2013), we used $l = 500$ m and obtained the London city cluster (Fig. 1a).
2) A belt of approximately equal size as the cluster was determined by consecutively enclosing layers of nonurban land use, avoiding other urban cells (Zhou et al. 2013, their supplementary material).
3) Based on the gridded temperature fields, we calculated the average temperatures in the cluster T_C and in the belt T_B. The temperature is either LST from MODIS or modeled 2-m air temperatures as described in section 2. The UHI intensity was then calculated as $\Delta T = T_C - T_B$. In any case, the resolution is 1 km, consistent with that used in MODIS. Figure 1b shows, as an example, the annual mean 2-m air temperature map from the UrbClim model.

The 2006 CORINE land cover data used in this study include 38 European Environmental Agency member states (Büttner et al. 2007). The 44 distinguished land surface classes include artificial land coverage and are reclassified into urban and nonurban in accordance with Simon et al. (2010).

We used the MOD11A2 and MYD11A2 version-5 data from the MODIS *Terra* and *Aqua* platforms,

TABLE 2. Error statistics for the simulated (vs observed) urban (T_u; St. James Park) and rural (T_r; Charlwood) 2-m air temperatures and their differences (ΔT). The quantities given are the bias, root-mean-square error (RMSE), and correlation coefficient (CORR).

	T_u			T_r			ΔT		
Year	Bias	RMSE	CORR	Bias	RMSE	CORR	Bias	RMSE	CORR
2010	0.08	0.73	0.99	0.01	0.64	0.99	0.07	0.29	0.70
2011	0.26	0.93	0.99	0.17	0.91	0.98	0.17	0.42	0.59
2012	0.12	0.87	0.99	0.05	0.98	0.98	0.07	0.36	0.65

respectively. Determined by overpass times, the *Terra* satellite provides twice-daily data at around 1030 and 2230 LT, while the *Aqua* data are collected at 1330 and 0130 LT. Both data are aggregated into an 8-day temporal resolution, which corresponds to 46 observations annually. Wan (2008) validated LST version-5 data with in situ measurements, indicating an accuracy better than 1°C in most cases.

By averaging the four periods of MODIS data for each observation, we obtained gridded temperature fields of daily means. To minimize bias caused by cloud contamination inherent in the data, we based our calculation of each grid cell only on complete data. Gridded daily means based on incomplete data are omitted. Unless specified differently, we use daily averages for our analyses hereafter. Moreover, we disregarded observations where either cluster or belt was affected by at least 50% cloud cover. Finally, we had 276 valid observations (86% of the total) from 2006 to 2012 (the UrbClim simulations were run over the same period).

We plotted the UHI intensity ΔT as a function of the background temperature T_B and calculated the monthly averages of both quantities. To better assess the hysteresis, we performed a second-order Fourier approximation of both times series, in agreement with Zhou et al. (2013).

4. Results

a. *Observed and modeled 2-m air temperature comparison*

The UrbClim model has already been successfully validated regarding its energy fluxes, 2-m air temperatures, and urban–rural temperature differences for the cities of Ghent (Belgium) and Toulouse (France; De Ridder et al. 2015). The LST in the UrbClim land surface scheme has also been validated in the past with satellite data. In De Ridder (2006), the urban parameterization is tested for the city of Paris, and the simulated LST compared favorably to observed values obtained from thermal infrared satellite imagery. Afterward, the land surface scheme was coupled to a mesoscale atmospheric model and applied to both Paris and the German Ruhr area, again yielding good comparisons between simulated and observed LST from thermal infrared satellite imagery (De Ridder et al. 2008, 2012).

Regarding the London domain in this study, we were able to obtain 2-m air temperature measurement data from a location inside the city center (St. James Park; 51.504°N, 0.129°W) and in the rural surroundings (Charlwood; 51.144°N, 0.230°W) for the period 2010–12. Unfortunately, the urban station is located inside a park, which is known to be cooler than a true urban environment, so the measurements do not capture the full extent of the London UHI effect. To obtain comparable statistics as in the LST analysis, the data were aggregated into an 8-day temporal resolution that corresponded to 46 observations each year. The error statistics of the UrbClim model for both locations are shown in Table 2. The overall performance of the model is good, with a bias of only a few tenths of a degree, root-mean-square errors below 1°C, and correlation coefficients above 0.98.

However, the focus of this evaluation is on the model's ability to reproduce observed urban–rural temperature differences. The simulated temperature differences agree fairly well with the observed ones, with a negligible bias, a root-mean-square error below 0.5°C, and correlation coefficients up to 0.7.

To evaluate the model's ability to reproduce the spatial pattern of 2-m air temperatures, measurement data from six additional locations in and around the city were gathered for the year 2011. The locations of the measurement stations are shown in Fig. 1b, with the annual mean 2-m air temperature from the UrbClim model in the background. Figure 1c depicts the linear relationship between modeled and observed values, with a bias of 0.22 and a coefficient of determination R^2 of 0.90, suggesting the model can properly reproduce the observation regarding its annual mean spatial pattern.

b. *Observed and modeled land surface temperature comparison*

We calculated the LST UHI intensity for London from measurements as detailed in section 3, which we compare in the following with the results of the

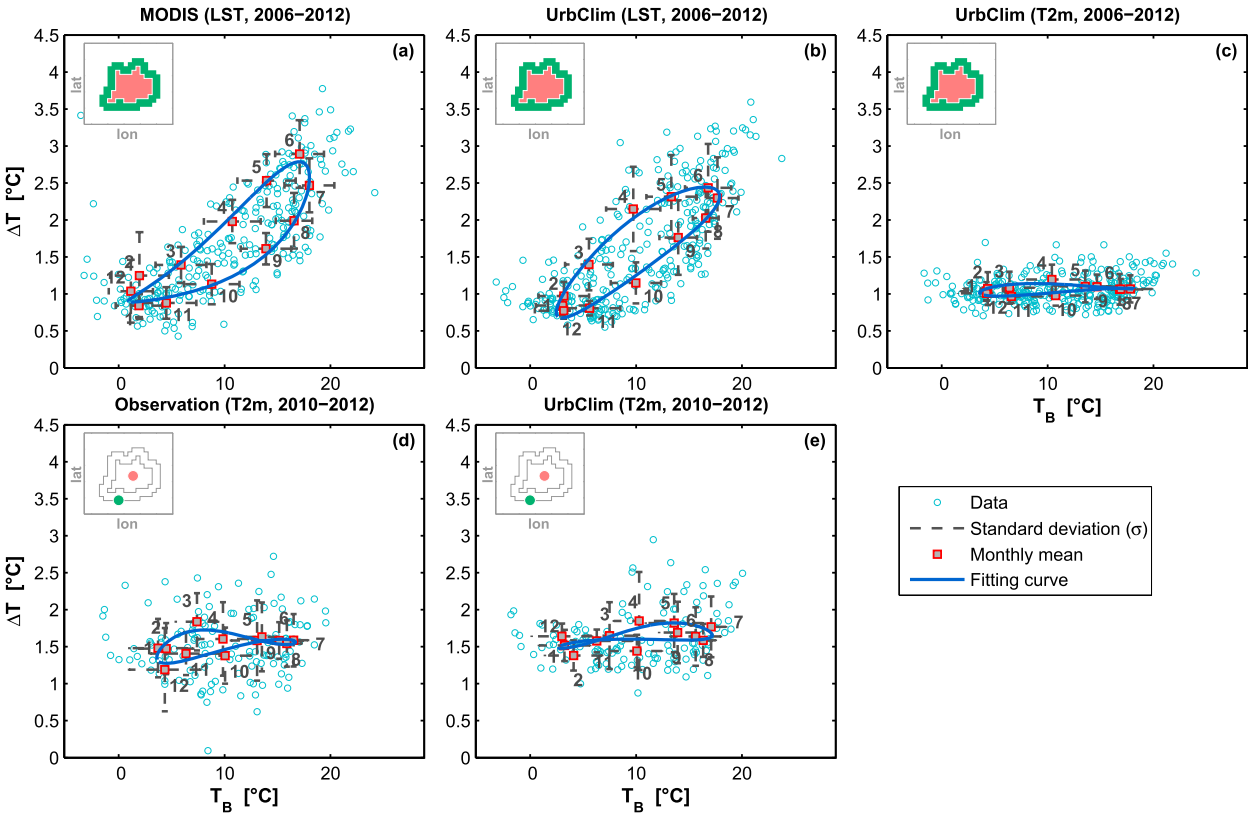

FIG. 2. Seasonality of UHI intensity for the London city cluster based on empirical MODIS (LST), observations (2-m temperatures), and modeled UrbClim results (both). The inset icons denote how the UHI intensity (ΔT) is calculated, that is, based either (a)–(c) on the mean temperature difference between urban area and its surroundings or (d),(e) on the temperature difference between St. James Park (urban) and Charlwood (rural). The UHI intensity ΔT is plotted as a function of the background temperature T_B. The numbers (1–12) within the plot correspond to months of the year. Panels (a) and (b) show the results for land surface temperatures, whereas (c)–(e) are for the 2-m air temperatures. The comparison between the observed and modeled 2-m air temperatures [in (d) and (e)] is based on data from 2010 to 2012.

UrbClim model (see section 2). Empirical and modeled temperatures have spatial and temporal overlap, and we calculate the UHI intensities in the analogous manner.

First, we want to analyze if the UrbClim model reproduces the hysteresis-like seasonality in the LST. Therefore, the UHI intensity ΔT is plotted versus the background temperature T_B. For both quantities, the raw data in 8-day resolution are aggregated to monthly means.

Figure 2 exhibits the raw values, the monthly means with standard deviations, and second-order Fourier approximation. Figures 2a and 2b show the LST results for the MODIS data and the UrbClim model, respectively. In the case of the measured data, the monthly background temperature ranges between slightly over 0°C and almost 20°C, whereas the UHI intensity is between somewhat lower than 1°C and almost 3°C. The modeled data show similar ranges, although slightly smaller UHI intensity in summer and slightly higher background temperature in winter.

Despite considerable spreading of the 8-day values, the monthly values exhibit the characteristic clockwise course in both Figs. 2a and 2b, which imply a phase shift between the UHI intensity and the background temperature. The UHI intensity reaches its peak around the summer solstice, that is, in the strongest incoming solar radiation, while the maximum values of background temperature occur around the end of July and the beginning of August. As can be seen in Fig. 2a, the typical UHI intensity in May is larger than in September by approximately 1°C. The modeled data in Fig. 2b show a similar effect, although a bit less pronounced in May–September. Overall, the hysteresis-like seasonality in the modeled LST matches the observed pattern for London. The differences in the shape of the Fourier approximations are minor compared to the spreading of the raw data and the resulting standard deviations.

The simulated 8-day averaged LST agrees with the observations, both for the city cluster and the belt (Table 3). The UrbClim model also performs well in

TABLE 3. Error statistics for the simulated 8-day averaged LST vs observed MODIS LST for urban cluster T_C, belt T_B, and their difference ΔT.

	T_C	T_B	ΔT
Bias	0.18	0.21	−0.03
RMSE	1.19	1.23	0.40
CORR	0.99	0.98	0.86

simulating the LST-based UHI, with a bias of −0.03 and a correlation coefficient of 0.86.

c. *Modeled land surface and 2-m air temperature comparison*

The described hysteresis-like seasonality has been reported and reproduced (section 4b) only for land surface temperature so far. Next, we want to verify if the phenomenon occurs also in the 2-m air temperature.

First, we investigate if the hysteresis is present in the measurement data from the stations St. James Park and Charlwood for the years 2010–12 and if the UrbClim model shows comparable results. Afterward, we focus on the full modeled period (2006–12) to make a comparison with the LST analysis. The comparison between measurements and model results regarding a potential hysteresis-like seasonality is presented in Figs. 2d and 2e. A hysteresis-like seasonality is absent in both the observations and the model results, as all year round the UHI intensity for 2-m air temperatures is between 1° and 2°C.

Figures 2b and 2c show the results for the modeled LST and 2-m air temperature, respectively. Here, we calculate the daily mean temperature by averaging the four times of the day. While the background temperature T_B exhibits a similar range in both cases, it is apparent that the modeled 2-m air temperature is not significantly different between the seasons. The maximum deviation of approximately 0.2°C occurs between April and October (Fig. 2c). In comparison to the size of the spreading, this effect can be neglected.

As we do not observe any significant hysteresis-like seasonality in the daily mean 2-m air temperature in both the model and the observations, we can conclude that it must be a phenomenon that is restricted to land surface temperature. In other words, the UHI intensities derived from LST and air temperature constitute different seasonalities.

In Fig. 2c, ΔT is approximately constant throughout the year. Under the climate conditions, relatively high UHI episodes can occur, even in winter, during dry and sunny periods. Since sunny episodes and rainfall events are possible all over the year, ΔT is almost constant.

d. *Seasonality of daytime and nighttime UHI intensities*

Figure 3 shows the seasonality of air-temperature-based UHI for both daytime and nighttime. It is generally known that the nighttime UHI is larger than the daytime UHI for air temperatures (Oke 1987). The UHI intensity reaches its peak of about 2°C at 0130 LT in spring (April–May), whereas the minimum UHI intensity occurs at 1330 LT (about 0.5°C). On clear-sky days, during the daytime, the surface is heated by solar radiation, and the boundary layer becomes unstable, favoring convection and turbulent mixing. This mixing hampers the formation of a strong near-surface UHI since a lot of warm air is transported upward to the atmosphere. After sunset, the surface cools and the boundary layer becomes stable, favoring stronger near-surface temperature gradients. The difference in cooling rate between urban and rural area further intensifies the UHI. This process might explain the bimodal seasonality at 2230 LT. Because of the late sunset time (about 2120 LT) in June and July, the stabilization of the boundary layer occurs after 2230 LT. The UHI intensity reaches its peak several hours after sunset and at 0130 LT is approximately 0.4°C larger than at 2230 LT in June–July.

Table 4 shows the partial correlation matrix of UHI intensities for different times of the day. For LST-based UHI intensities, from both observation and simulation, highly positive correlations are found between individual times of the day (shown in the left and center matrices of Table 4). For air-temperature-based UHI intensities, high correlations are found solely between daytime UHI intensities (1030 and 1330 LT) and between nighttime UHI intensities (0130 and 2230 LT), whereas nonsignificant and even negative correlations are found between daytime and nighttime UHI intensities. This difference suggests that the LST-based UHI intensities exhibit similar seasonalities at various times during the day, while this consistency across times does not exist with respect to air-temperature-based UHI intensities. When averaging to daily mean, the air-temperature-based UHI seasonality is attenuated. This could explain why the LST-based daily mean UHI exhibits a pronounced seasonality throughout the study period, whereas a similar trend is absent for the air-temperature-based UHI.

A previous study conducted by Wilby (2003) assessed both daytime and nighttime UHI intensities based on 2-m air temperature data observed from 1961 to 1990 at two weather stations (St. James

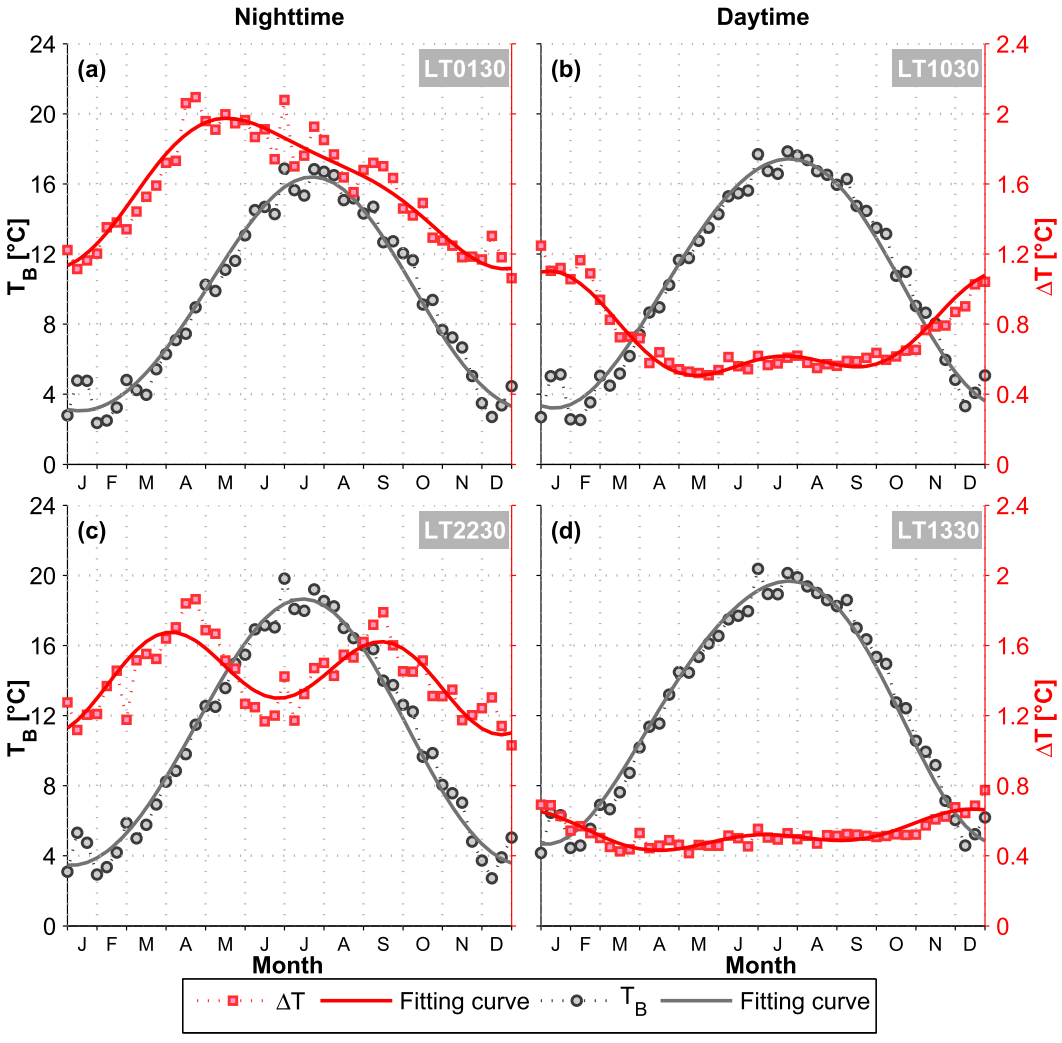

FIG. 3. The seasonality of modeled air temperature. Background temperatures T_B and UHI intensities ΔT are shown for four local times of the day, (a) 0130, (b) 1030, (c) 1330, and (d) 2230 LT, that are consistent with the MODIS overpass times. The data are fitted by second-order Fourier approximations.

Park and Wisley, 30 km from London). He reported a maximum nighttime UHI intensity in August (2.2°C) and a minimum in January (1.1°C), whereas there was no remarkable seasonality in the daytime UHI intensity. We recalculated the UHI intensity in a similar way to Wilby (2003), that is, defining the nighttime UHI intensity as $\Delta T_{\min} = \min(T_C^t) - \min(T_B^t)$, $t \in \{\text{LT0130, LT2230}\}$, and the daytime UHI as $\Delta T_{\max} = \max(T_C^t) - \max(T_B^t)$, $t \in \{\text{LT1030, LT1330}\}$. As can be seen from Figs. 4a and 4b, in the present study the daytime UHI intensities have low values (about 0.5°C) throughout the year, whereas the nighttime UHI intensity reaches its maximum in April–May (about 2.0°C). Considering the difference in study period, UHI definition, and large data spreading in the previous study, it is reasonable to conclude that our findings are consistent and well comparable with the previous ones.

e. *Sensitivity to the annual cycle in the radiation*

We found that UrbClim reproduces the hysteresis-like seasonality in the LST-based UHI and that the effect is largely absent in the 2-m air temperature UHI (section 4c). Next, we want to investigate a possible mechanism behind the hysteresis-like seasonality. It has been hypothesized that the phenomenon is due to the phase shift between astronomical and meteorological seasons: the land surface temperature in the city follows the astronomical seasons driven by solar radiation, and the temperature in the surroundings follows the meteorological seasons corresponding to the regional climate (Zhou et al. 2013).

TABLE 4. Correlations between UHI intensities of four individual times, based on MODIS-observed LST ($\Delta T_{\mathrm{LST}}^{\mathrm{MODIS}}$), UrbClim simulated LST ($\Delta T_{\mathrm{LST}}^{\mathrm{UrbClim}}$), and UrbClim simulated 2-m air temperature ($\Delta T_{T_{2\mathrm{m}}}^{\mathrm{UrbClim}}$). For LST-based UHI intensities, from both observation and simulation, highly positive correlations are found between individual times of the day, whereas for air-temperature-based UHI intensities, correlations are nonsignificant or even negative between different times. Asterisks represent $p > 0.01$.

$\Delta T_{\mathrm{LST}}^{\mathrm{MODIS}}$				$\Delta T_{\mathrm{LST}}^{\mathrm{UrbClim}}$				$\Delta T_{T_{2\mathrm{m}}}^{\mathrm{UrbClim}}$			
LT 0130				LT 0130				LT 0130			
0.62	LT 1030			0.92	LT 1030			−0.26	LT 1030		
0.63	0.89	LT 1330		0.94	0.95	LT 1330		−0.11*	0.66	LT 1330	
0.71	0.65	0.65	LT 2230	0.95	0.87	0.93	LT 2230	0.74	−0.04*	−0.03*	LT 2230

Here, we test this hypothesis by performing a model run with manipulated external driving. As detailed in section 2b, in the sensitivity experiment the clear-sky maximum shortwave radiation (SR experiment) is kept constant throughout the year. In Fig. 5, we compare the LST UHI intensities of MODIS with the ones obtained from the SR experiment. While in Fig. 2 the daily averages are plotted, in Fig. 5 we study the four times of the day separately.

During the daytime it can be seen that the hysteresis shape greatly diminishes in the manipulated model run and only small UHI intensities in the LST remain, in contrast to the unaltered data observed with large maximum ΔT of approximately 4°C in June. During the nighttime, however, the UHI intensities of the SR experiment still exhibit a slight hysteresis shape, in contrast to the nighttime of the MODIS data, where the phenomenon does not occur. This remaining hysteresis at night could be due to a combination of the higher soil moisture and colder deep soil temperatures in spring, compared to autumn, keeping the rural LST low and therefore increasing the UHI effect. Indeed, observations indicate a seasonality in the soil moisture content in the London region, which results in larger thermal admittance and a decrease of warming rate in the rural areas in spring relative to autumn. Figure 6 shows the 7-yr (2006–12) monthly mean soil moisture for the Greater London area, obtained from the NOAA Climate Prediction Center (CPC) soil moisture data (Fan 2004). However, the UrbClim model appears to be too sensitive to this effect, as it cannot be seen in the nighttime MODIS data. During daytime the seasonality of soil moisture plays a minor role in the hysteresis effect, as the astronomical seasonality is dominant.

5. Summary and discussion

In this paper we have analyzed the seasonal variation of UHI intensities by combining satellite-based observations from MODIS and simulations with the urban boundary layer climate model UrbClim. Based on both LST and 2-m air temperature, the seasonality of UHI intensity from 2006 to 2012 has been investigated. Although both are supposed to describe the magnitude of city warming compared to the surrounding, they constitute different seasonalities. We find that the model reproduces the hysteresis effect in the surface UHI intensities. In the observed and modeled 2-m air temperature, the phenomenon is largely absent, suggesting that the seasonality is due to peculiarities of the LST. Both observed and simulated LST-based UHI intensities exhibit consistent seasonality across the different times of the day. However, the seasonality of UHI intensities based on air temperature is rather a function of the time of the day.

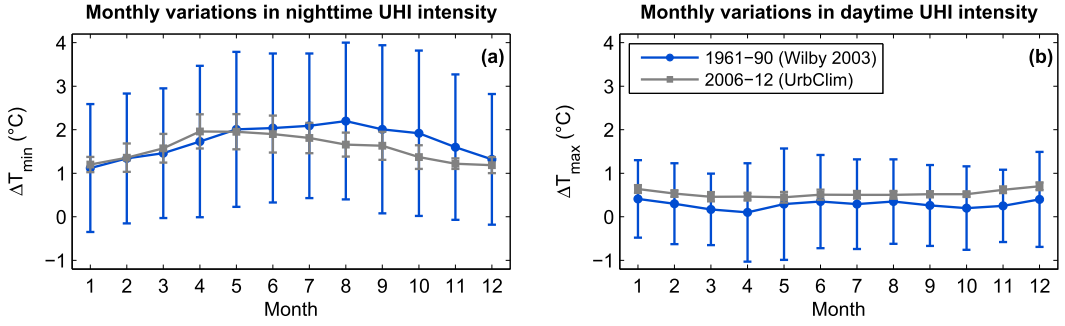

FIG. 4. Monthly variations in (a) nighttime and (b) daytime UHI intensities based on 2-m air temperature modeled by UrbClim in comparison with the results by Wilby (2003), where observational temperature data from two weather stations from 1961 to 1990 were used to calculate the UHI intensities. Vertical bars denote standard deviations.

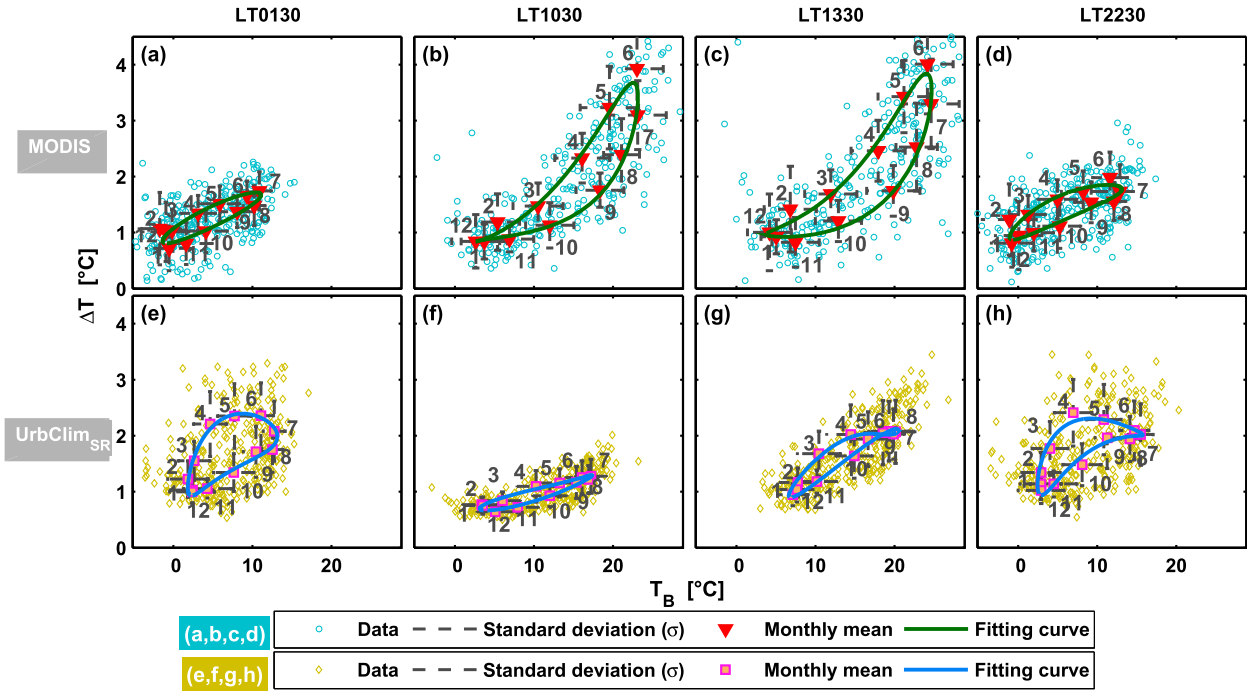

FIG. 5. Hysteresis of UHI intensity for the London city cluster comparing the empirical MODIS values with the ones obtained from the constant SR experiment as explained in section 2b. Analogous to Fig. 2, the UHI intensity ΔT is plotted as a function of the background temperature T_B for (top) MODIS and (bottom) UrbClim SR experiment. The numbers (1–12) within the plot correspond to months of the year. The columns show the results for the four local times of the day: (a),(e) 0130; (b),(f) 1030; (c),(g) 1330; and (d), (h) 2230.

A sensitivity test has been conducted by rescaling the incoming shortwave radiation so that the clear-sky maximum radiation is always equal to the value of 21 March. In this case, the surface UHI intensity is considerably reduced, supporting that the hysteresis is due to a delay between the meteorological seasonality, driving the background temperature, and the astronomical seasonality, driving the city temperature.

In future work it could be of interest to relate this perception with the earlier findings by Runnalls and Oke (2000). They suggested that seasonalities of UHI intensity could be mainly attributed to the difference in thermal admittance between urban and rural areas, which determines the warming and cooling rate of each part. For urban areas, the thermal admittance could be seen as constant throughout the year. The warming rate of urban areas is proportional to the solar radiation during the daytime, while its cooling rate due to infrared emission is almost constant during the nighttime. In the nonurban area, where the thermal admittance is highly subject to soil moisture and vegetation, the warming and cooling rates exhibit pronounced seasonal variations. Around the summer solstice the urban warming rate reaches its maximum and so is the difference between urban and rural warming. As a consequence of this difference, the UHI intensity peaks in June–July.

Our results indicate that the seasonality of the soil moisture in the London region can contribute to seasonal variations of the UHI intensity. Although this effect is less pronounced in the case of London, we expect that larger differences (e.g., in more semiarid conditions) could contribute significantly to hysteresis-like curves in other regions.

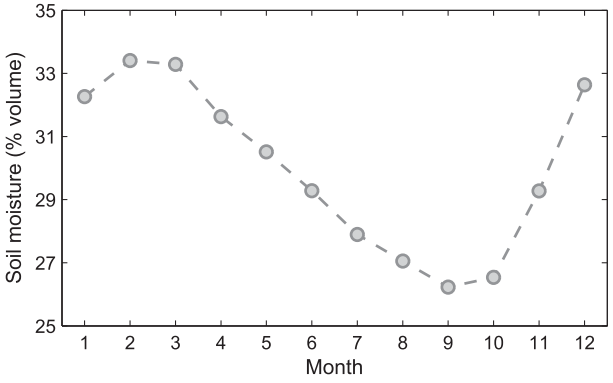

FIG. 6. Monthly means of soil moisture for London, derived from NOAA CPC soil moisture data at a 0.5° × 0.5° grid.

Acknowledgments. The research leading to these results has received funding from the European Community's Seventh Framework Programme under Grant Agreement 308497 (Project RAMSES). The authors thank David Landholm and three anonymous reviewers for helpful comments on the manuscript. Author BZ thanks Climate-KIC, the climate innovation initiative of the EU's European Institute of Innovation and Technology (EIT), for award of a Ph.D. scholarship. We acknowledge the EEA for making available the CORINE land cover data and NASA LP DAAC for the MODIS LST data. CPC soil moisture data are provided by the NOAA/OAR/ESRL PSD, Boulder, Colorado, from their website at http://www.esrl.noaa.gov/psd/.

REFERENCES

Arnfield, J., 2003: Two decades of urban climate research: A review of turbulence, exchanges of energy and water, and the urban heat island. *Int. J. Climatol.*, **23**, 1–26, doi:10.1002/joc.859.

Büttner, G., T. Soukup, and A. Sousa, 2007: CLC2006 technical guidelines. Tech. Rep. 17, European Environment Agency, 66 pp., doi:10.2800/12134.

Cui, Y. Y., and B. de Foy, 2012: Seasonal variations of the urban heat island at the surface and the near-surface and reductions due to urban vegetation in Mexico City. *J. Appl. Meteor. Climatol.*, **51**, 855–868, doi:10.1175/JAMC-D-11-0104.1.

Danielson, J. J., and D. B. Gesch, 2011: Global multi-resolution terrain elevation data 2010 (GMTED2010). USGS Open-File Rep. 2011-1073, 26 pp. [Available online at http://pubs.usgs.gov/of/2011/1073/pdf/of2011-1073.pdf.]

De Ridder, K., 2006: Testing Brutsaert's temperature roughness parameterization for representing urban surfaces in atmospheric models. *Geophys. Res. Lett.*, **33**, L13403, doi:10.1029/2006GL026572.

——, and G. Schayes, 1997: The IAGL land surface model. *J. Appl. Meteor.*, **36**, 167–182, doi:10.1175/1520-0450(1997)036<0167:TILSM>2.0.CO;2.

——, and Coauthors, 2008: Simulating the impact of urban sprawl on air quality and population exposure in the German Ruhr area. Part I: Reproducing the base state. *Atmos. Environ.*, **42**, 7059–7069, doi:10.1016/j.atmosenv.2008.06.045.

——, C. Bertrand, G. Casanova, and W. Lefebvre, 2012: Exploring a new method for the retrieval of urban thermophysical properties using thermal infrared remote sensing and deterministic modeling. *J. Geophys. Res.*, **117**, D17108, doi:10.1029/2011JD017194.

——, D. Lauwaet, and B. Maiheu, 2015: Urbclim—A fast urban boundary layer climate model. *Urban Climate*, **12**, 21–48, doi:10.1016/j.uclim.2015.01.001.

Estournel, C., R. Vehil, D. Guedalia, J. Fontan, and A. Druilhet, 1983: Observations and modeling of downward radiative fluxes (solar and infrared) in urban/rural areas. *J. Climate Appl. Meteor.*, **22**, 134–142, doi:10.1175/1520-0450(1983)022<0134:OAMODR>2.0.CO;2.

Fan, Y., 2004: Climate Prediction Center global monthly soil moisture data set at 0.5° for 1948 to present. *J. Geophys. Res.*, **109**, D10102, doi:10.1029/2003JD004345.

Figuerola, P. I., and N. A. Mazzeo, 1998: Urban-rural temperature differences in Buenos Aires. *Int. J. Climatol.*, **18**, 1709–1723, doi:10.1002/(SICI)1097-0088(199812)18:15<1709::AID-JOC338>3.0.CO;2-I.

Gallo, K., R. Hale, D. Tarpley, and Y. Yu, 2011: Evaluation of the relationship between air and land surface temperature under clear- and cloudy-sky conditions. *J. Appl. Meteor. Climatol.*, **50**, 767–775, doi:10.1175/2010JAMC2460.1.

Garratt, J. R., 1992: *The Atmospheric Boundary Layer.* Cambridge University Press, 316 pp.

Gutman, G., and A. Ignatov, 1998: The derivation of the green vegetation fraction from NOAA/AVHRR data for use in numerical weather prediction models. *Int. J. Remote Sens.*, **19**, 1533–1543, doi:10.1080/014311698215333.

Ichinose, T., K. Shimodozono, and K. Hanaki, 1999: Impact of anthropogenic heat on urban climate in Tokyo. *Atmos. Environ.*, **33**, 3897–3909, doi:10.1016/S1352-2310(99)00132-6.

Imhoff, M. L., P. Zhang, R. E. Wolfe, and L. Bounoua, 2010: Remote sensing of the urban heat island effect across biomes in the continental USA. *Remote Sens. Environ.*, **114**, 504–513, doi:10.1016/j.rse.2009.10.008.

Jauregui, E., 1997: Heat island development in Mexico City. *Atmos. Environ.*, **31**, 3821–3831, doi:10.1016/S1352-2310(97)00136-2.

Jin, M., and R. E. Dickinson, 2010: Land surface skin temperature climatology: Benefitting from the strengths of satellite observations. *Environ. Res. Lett.*, **5**, 044004, doi:10.1088/1748-9326/5/4/044004.

Kalnay, E., and M. Cai, 2003: Impact of urbanization and land-use change on climate. *Nature*, **423**, 528–531, doi:10.1038/nature01675.

Kanda, M., M. Kanega, T. Kawai, R. Moriwaki, and H. Sugawara, 2007: Roughness lengths for momentum and heat derived from outdoor urban scale models. *J. Appl. Meteor. Climatol.*, **46**, 1067–1079, doi:10.1175/JAM2500.1.

Kim, Y.-H., and J.-J. Baik, 2005: Spatial and temporal structure of the urban heat island in Seoul. *J. Appl. Meteor.*, **44**, 591–605, doi:10.1175/JAM2226.1.

Norman, J. M., and F. Becker, 1995: Terminology in thermal infrared remote sensing of natural surfaces. *Remote Sens. Rev.*, **12**, 159–173, doi:10.1080/02757259509532284.

Nunez, M., I. Eliasson, and J. Lindgren, 2000: Spatial variations of incoming longwave radiation in Göteborg, Sweden. *Theor. Appl. Climatol.*, **67**, 181–192, doi:10.1007/s007040070007.

Oke, T. R., 1982: The energetic basis of the urban heat island. *Quart. J. Roy. Meteor. Soc.*, **108**, 1–24, doi:10.1002/qj.49710845502.

——, 1987: *Boundary Layer Climates.* 2nd ed. Methuen, 435 pp.

——, G. T. Johnson, D. G. Steyn, and I. D. Watson, 1991: Simulation of surface urban heat islands under 'ideal' conditions at night part 2: Diagnosis of causation. *Bound.-Layer Meteor.*, **56**, 339–358, doi:10.1007/BF00119211.

Parker, D. E., 2010: Urban heat island effects on estimates of observed climate change. *Wiley Interdiscip. Rev. Climate Change*, **1**, 123–133, doi:10.1002/wcc.21.

Peng, S., and Coauthors, 2012: Surface urban heat island across 419 global big cities. *Environ. Sci. Technol.*, **46**, 696–703, doi:10.1021/es2030438.

Pielke, R. A., Sr., 2002: *Mesoscale Meteorological Modeling.* 2nd ed. International Geophysics Series, Vol. 78, Academic Press, 676 pp.

Piringer, M., and Coauthors, 2007: The surface energy balance and the mixing height in urban areas—Activities and recommendations of COST-Action 715. *Bound.-Layer Meteor.*, **124**, 3–24, doi:10.1007/s10546-007-9170-0.

Pongrácz, R., J. Bartholy, and Z. Dezs, 2010: Application of remotely sensed thermal information to urban climatology of Central European cities. *Phys. Chem. Earth*, **35**, 95–99, doi:10.1016/j.pce.2010.03.004.

Prigent, C., A. Filipe, and B. R. William, 2003: Land surface skin temperatures from a combined analysis of microwave and infrared satellite observations for an all-weather evaluation of the differences between air and skin temperatures. *J. Geophys. Res.*, **108**, 4310, doi:10.1029/2002JD002301.

Roth, M., 2007: Review of urban climate research in (sub)tropical regions. *Int. J. Climatol.*, **27**, 1859–1873, doi:10.1002/joc.1591.

Rouse, W. R., D. Noad, and J. McCutcheon, 1973: Radiation, temperature and atmospheric emissivities in a polluted urban atmosphere at Hamilton, Ontario. *J. Appl. Meteor.*, **12**, 798–807, doi:10.1175/1520-0450(1973)012<0798:RTAAEI>2.0.CO;2.

Rozenfeld, H. D., D. Rybski, J. S. Andrade Jr., M. Batty, H. E. Stanley, and H. A. Makse, 2008: Laws of population growth. *Proc. Natl. Acad. Sci. USA*, **105**, 18 702–18 707, doi:10.1073/pnas.0807435105.

——, ——, X. Gabaix, and H. A. Makse, 2011: The area and population of cities: New insights from a different perspective on cities. *Amer. Econ. Rev.*, **101**, 2205–2225, doi:10.1257/aer.101.5.2205.

Runnalls, K., and T. Oke, 2000: Dynamics and controls of the near-surface heat island of Vancouver, British Columbia. *Phys. Geogr.*, **21**, 283–304, doi:10.1080/02723646.2000.10642711.

Sailor, D. J., and L. Lu, 2004: A top-down methodology for developing diurnal and seasonal anthropogenic heating profiles for urban areas. *Atmos. Environ.*, **38**, 2737–2748, doi:10.1016/j.atmosenv.2004.01.034.

Schatz, J., and C. J. Kucharik, 2014: Seasonality of the urban heat island effect in Madison, Wisconsin. *J. Appl. Meteor. Climatol.*, **53**, 2371–2386, doi:10.1175/JAMC-D-14-0107.1.

Simon, A., J. Fons, R. Milego, and B. Georgi, 2010: Urban Morphological Zones version F2v0: Definition and procedural steps. Final rep., ETC/LUSI and EEA, 27 pp. [Available online at http://www.eea.europa.eu/data-and-maps/data/urban-morphological-zones-1990/note/note/download.]

Stewart, I. D., and T. R. Oke, 2012: Local climate zones for urban temperature studies. *Bull. Amer. Meteor. Soc.*, **93**, 1879–1900, doi:10.1175/BAMS-D-11-00019.1.

Tomlinson, C. J., L. Chapman, J. E. Thornes, and C. Baker, 2011: Remote sensing land surface temperature for meteorology and climatology: A review. *Meteor. Appl.*, **18**, 296–306, doi:10.1002/met.287.

Tran, H., D. Uchihama, S. Ochi, and Y. Yasuoka, 2006: Assessment with satellite data of the urban heat island effects in Asian mega cities. *Int. J. Appl. Earth Obs. Geoinf.*, **8**, 34–48, doi:10.1016/j.jag.2005.05.003.

UN-HABITAT, 2011: *Cities and Climate Change: Global Report on Human Settlements 2011*. UN-HABITAT, 300 pp.

Unger, J., Z. Sümeghy, and J. Zoboki, 2001: Temperature cross-section features in an urban area. *Atmos. Res.*, **58**, 117–127, doi:10.1016/S0169-8095(01)00087-4.

Voogt, J., and T. Oke, 2003: Thermal remote sensing of urban climates. *Remote Sens. Environ.*, **86**, 370–384, doi:10.1016/S0034-4257(03)00079-8.

Wan, Z., 2008: New refinements and validation of the MODIS Land-Surface Temperature/Emissivity products. *Remote Sens. Environ.*, **112**, 59–74, doi:10.1016/j.rse.2006.06.026.

Weng, Q., 2009: Thermal infrared remote sensing for urban climate and environmental studies: Methods, applications, and trends. *ISPRS J. Photogramm. Remote Sens.*, **64**, 335–344, doi:10.1016/j.isprsjprs.2009.03.007.

Wilby, R. L., 2003: Past and projected trends in London's urban heat island. *Weather*, **58**, 251–260, doi:10.1256/wea.183.02.

Wouters, H., M. Demuzere, K. De Ridder, and N. P. M. van Lipzig, 2015: The impact of impervious water-storage parametrization on urban climate modelling. *Urban Climate*, **11**, 24–50, doi:10.1016/j.uclim.2014.11.005.

Zhou, B., D. Rybski, and J. P. Kropp, 2013: On the statistics of urban heat island intensity. *Geophys. Res. Lett.*, **40**, 5486–5491, doi:10.1002/2013GL057320.

Zhou, Y., and J. M. Shepherd, 2010: Atlanta's urban heat island under extreme heat conditions and potential mitigation strategies. *Nat. Hazards*, **52**, 639–668, doi:10.1007/s11069-009-9406-z.